Reaction Chemistry & Engineering

ROYAL SOCIETY OF CHEMISTRY

PAPER

View Article Online
View Journal | View Issue

Cite this: *React. Chem. Eng.*, 2020, 5, 696

An experimental, theoretical and kinetic-modeling study of the gas-phase oxidation of ammonia†

Alessandro Stagni, *[a] Carlo Cavallotti, [a] Suphaporn Arunthanayothin,[b] Yu Song,[bc] Olivier Herbinet, [b] Frédérique Battin-Leclerc [b] and Tiziano Faravelli [a]

A complete understanding of the mechanism of ammonia pyrolysis and oxidation in the full range of operating conditions displayed by industrial applications is one of the challenges of modern combustion kinetics. In this work, a wide-range investigation of the oxidation mechanism of ammonia was performed. Experimental campaigns were carried out in a jet-stirred reactor and a flow reactor under lean conditions ($0.01 \leq \Phi \leq 0.375$), such to cover the full range of operating temperatures ($500\ K \leq T \leq 2000\ K$). Ammonia conversion and the formation of products and intermediates were analyzed. At the same time, the ammonia decomposition reaction, H-abstractions and the decomposition of the HNO intermediate were evaluated *ab initio*, and the related rates were included in a comprehensive kinetic model, developed according to a first-principles approach. Low-temperature reactor experiments highlighted a delayed reactivity of ammonia, in spite of the high amount of oxygen. A very slow increase in NH_3 consumption rate with temperature was observed, and a full reactant consumption was possible only ~150–200 K after the reactivity onset. The use of flux analysis and sensitivity analysis allowed explaining this effect with the terminating effect of the H-abstraction on NH_3 by O_2, acting in the reverse direction because of the high amounts of HO_2. The central role of H_2NO was observed at low temperatures ($T < 1200$ K), and H-abstractions from it by HO_2, NO_2 and NH_2 were found to control reactivity, especially at higher pressures. On the other side, the formation of HNO intermediate *via* $NH_2 + O = HNO + H$ and its decomposition were found to be crucial at higher temperatures, affecting both NO/N_2 ratio and flame propagation.

Received 7th November 2019,
Accepted 22nd January 2020

DOI: 10.1039/c9re00429g

rsc.li/reaction-engineering

1 Introduction

The gradual transition towards newer and more sustainable energy sources for combustion applications is being carried out by pursuing two major targets: (i) a smarter, more efficient use of the available resources, in such a way to reduce energy wastes and CO_2 emissions, and (ii) a systematic control of pollutant emissions, which are formed as byproducts of the combustion processes. In this context, the scientific interest towards ammonia (NH_3) has been significantly increasing in the last years. As a matter of fact, the high energy density, ease of transportation and carbon-free nature of ammonia make it an attractive candidate as an energy vector: considering that its production relies on established production technologies as well as on a number of novel synthesis techniques,[1,2] NH_3 has also been proposed as a "platform molecule" for the energy storage from intermittent renewable sources (*i.e.* wind or sun), and based on successive release *via* either direct combustion or earlier conversion to hydrogen.[3] The competitiveness of ammonia as an energy carrier for the accumulation of excess energy and its release "on-demand" has been assessed in several works.[4,5] Moreover, its relevance in the next-generation energy scenario is also connected to its presence (in trace amounts) in biofuels: indeed, ammonia is found in biogas as a by-product of anaerobic digestion.[6,7] In addition, protein-rich sludges used as raw materials for bio-oils also contain NH_3 as well as other nitrogenated species.[8]

The research on the ammonia combustion chemistry actually started several decades ago. The high-temperature pyrolysis mechanism was first experimentally characterized starting from the 1980s,[9–12] with modelling work carried out in parallel.[12,13] Studies on oxidation focused first on NH_3 flame chemistry[14–16] and on its use within the Thermal $DeNO_x$ process[17] for the selective non-catalytic reduction of nitrogen oxides (NO_x). Later, oxidation chemistry was studied at a

[a] *Department of Chemistry, Materials, and Chemical Engineering "G. Natta", Politecnico di Milano, Milano 20133, Italy. E-mail: alessandro.stagni@polimi.it*
[b] *Laboratoire Réactions et Génie des Procédés, CNRS-Université de Lorraine, 1 rue Grandville, 54000 Nancy, France*
[c] *Laboratoire PRISME, Université d'Orléans, Polytech Vinci – 45072, Orléans, France*

† Electronic supplementary information (ESI) available. See DOI: 10.1039/c9re00429g

fundamental level through targeted experiments[18–20] and theoretical methodologies.[21–24] As a result, NH_3 kinetic mechanisms have largely benefited from incremental improvements. One of the first mechanisms was released by Miller *et al.*,[15] who later included NH_3 chemistry in their review work on nitrogen compounds.[25] Since then, many dedicated models describing ammonia combustion were released. Konnov and De Ruyck[26] extended the pyrolysis mechanism initially developed by Davidson *et al.*[12] by including the reactions of N_2H_3 and N_2H_4, which were shown to have an important effect on NH and NH_2 profiles. Mathieu and Petersen[27] extended the work of Dagaut *et al.*[28] on HCN chemistry to model the high-temperature ignition delay times of NH_3, collected under diluted conditions at different pressures and equivalence ratios. Shrestha *et al.*[29] recently presented a mechanism for the oxidation of NH_3 and NH_3/H_2 fuel blends, validated in several 0D and 1D systems, while Li *et al.*[30] developed two reduced mechanisms for the combustion of NH_3/H_2 and $NH_3/H_2/CH_4$ mixtures in air. The review work by Glarborg *et al.*[31] also includes ammonia pyrolysis and oxidation mechanism in their comprehensive nitrogen kinetic model, and provides an exhaustive overview of the state of the art in the kinetic modelling of NH_3 oxidation.

On the other hand, several experimental campaigns carried out in the latest years in less conventional conditions (lower temperatures, high dilution levels and wider pressure ranges) have shown that the fundamental knowledge of ammonia kinetics is still far from complete: the available mechanisms have shown important deviations in the autoignition behavior in diluted conditions, both in high-temperature shock tubes (ST)[27] and low- to intermediate-temperature shock tubes[32] and rapid compression machines (RCM).[33,34] Similarly, flow reactor experiments of pure NH_3 oxidation under atmospheric[35] and high pressure[36] showed that the kinetic models were not always able to reproduce the experimental trends. Da Rocha *et al.*[37] showed the inadequacy of several kinetic mechanisms in predicting the laminar flame speed (LFS) of NH_3, and most of them were shown to overpredict the actual rates.

In order to ensure an adequate degree of comprehensiveness, a fundamental understanding of ammonia kinetics still needs to be achieved. Glarborg *et al.*[31] pointed out the most unclear pathways of the NH_3 oxidation mechanism: they showed that the largest uncertainties are present under low-temperature conditions, especially with high concentrations of oxygen. In such cases, the role of intermediates, such as H_2NO and HNO, was shown to be determining, as well as the interaction of the HO_2 radical with the radical pool (*e.g.* NH_2 and NO). At the same time, the experimental data under these operating conditions in support of a proper model development are still very limited.

Starting from this scenario, the aim of this work is filling the void of knowledge still remaining in the kinetic mechanisms involved in the oxidation of ammonia, with a focus on the critical conditions previously mentioned, and scarcely explored so far. To this purpose, new experimental measurements were performed in a jet-stirred reactor (JSR) and a flow reactor (FR), such as to explore the low- and intermediate-temperature oxidation of ammonia with high dilution levels. At the same time, the critical rate constants involved in the ammonia combustion mechanism were systematically evaluated through a first-principles methodology. In particular, NH_3 decomposition, as well as H-abstractions by O_2, H, O, OH and HO_2, and the dissociation of the HNO intermediate are discussed. The calculated values were then exploited for a wide-range kinetic modeling of ammonia pyrolysis and oxidation, including the state-of-the-art kinetic constants made available in the latest years. This is used to interpret and explain the experimental results obtained in the two reactors. Finally, the comprehensive capability of the kinetic mechanism in predicting ammonia combustion in different configurations (ST, RCM, FR, LFS and Burner-Stabilized Flame - BSF) and operating conditions was assessed, highlighting the most critical competitive paths, still needing attention at a theoretical level.

2 Methodology

2.1 Experimental setup

The experimental measurements were performed using two different reactors, a jet-stirred reactor (JSR) and a tubular flow reactor (FR) working close to atmospheric pressure, in order to explore the low, intermediate and high temperature oxidation of ammonia with high dilution levels by using helium as carrier gas. Bronkhorst mass flow controllers are used for reactor feeding (relative uncertainty of ±0.5% in flow). Helium (99.999% pure) and O_2 (99.999%) were provided by Messer. A cylinder of 2004 ± 60 ppm ammonia diluted in helium, also provided by Messer, was used for the feed of ammonia.

In a first set-up, experiments were carried out in a fused silica JSR, a type of continuous stirred-tank reactor usually operated at steady state. JSRs were often used in gas phase kinetic studies. The present JSR setup was already described in previous works.[38–40] Briefly, it consisted of a spherical vessel with an injection of the preheated fresh mixture through four nozzles located at the center of the reactor, which produce high turbulence leading to homogeneity in temperature and composition. The preheating and heating of the reactor were performed using Inconel Thermocoax resistances rolled around the different parts and controlled by independent K-type thermocouples. A K-type thermocouple located in a glass finger close to the center of the reactor was used to measure the reaction temperature (uncertainty of ±5 K), which is considered as isothermal when running simulations. Pressure was set to 800 torr (106.7 kPa).

A second setup (Fig. 1) was specifically developed to explore NH_3 oxidation at higher temperature (up to ~2000 K) in a flow reactor (FR). It consisted of a tube made of recrystallized alumina (inner diameter of 4 mm and 100 cm in length), designed to approximate a plug flow reactor. Its operating pressure was 950 torr (126.7 kPa). Under the studied conditions, the Reynolds number was found to vary between

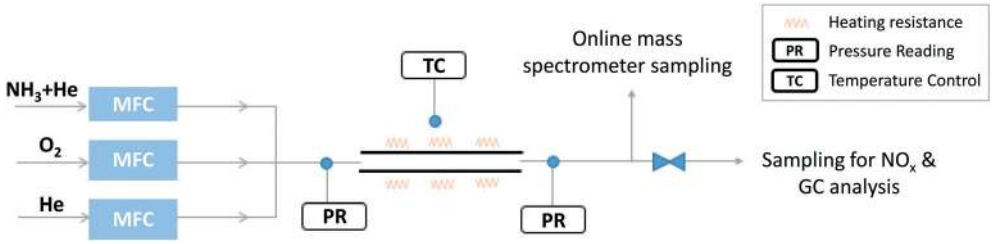

Fig. 1 Scheme of the experimental facility (flow reactor).

146 and 75, thus the flow was laminar. The Peclet number, Pe = $(u \times d)/D$ (u is the linear velocity of the gas, d is the internal diameter of the tube, and D is the molecular diffusivity of helium) was calculated as a function of temperature. The calculation provides values ranging from ~900 at ~1100 K to ~450 at ~2000 K, supporting the hypothesis that diffusion has a minor impact on the flow (Pe > 100) and that the reactor can be modelled as a plug flow reactor.[41]

The reactor was located horizontally in an electrically-heated oven (Carbolite Gero) which has an internal regulation. Actual temperature profiles were measured by an R-type thermocouple under unreactive conditions for each set-point temperature. Temperatures were recorded with a step of 2 cm in the isothermal region, and every 5 cm on both sides of the isothermal region. This isothermal reaction zone is located between 36 and 58 cm as shown in Fig. 2, with a quasi-uniform temperature profile (±30 K). The residence time is about 50 ms in the central zone where the temperature can be considered as constant. Flow rates were varied for each temperature set-point to maintain the residence time constants. Both temperature profiles and flow rate calculations are available as ESI.†

It is important to point out that significant catalytic effects of the reactor wall were first suspected in FR in the absence of oxygen when using non-recrystallized alumina. To confirm this, the following protocol was followed:

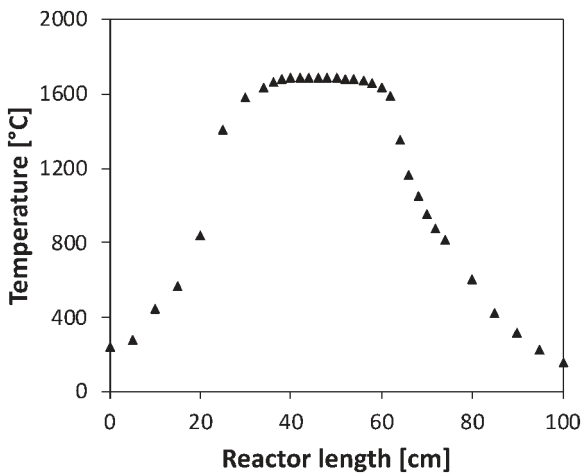

Fig. 2 Temperature profile measured (set point of 1700 °C) in the tubular flow reactor in absence of reaction.

1. Ammonia pyrolysis was first performed in a non-recrystallized alumina tube, in order to have a reference for comparison.

2. Then, the tube wall was coated with carbonaceous material by carrying out methane pyrolysis in the non-recrystallized alumina tube.

3. After coating, ammonia pyrolysis was repeated, and a significant shift of the reactivity of ~500 K towards lower temperatures was observed.

As a result, the tube was replaced and recrystallized alumina was adopted (with a higher purity than alumina). This resulted in a global shift of the reactivity of ~100 K towards higher temperatures when compared to the data obtained with the non-coated, non-recrystallized alumina first tube, and provided data consistent with model predictions.

Another evidence for the occurrence of wall interactions was the long time needed to reach steady state when flowing the reacting mixture (several tens of minutes). This was observed thanks to the use of online mass spectrometry with direct sampling in the gas phase at the outlet of the tube. Such stabilization time was considerably shortened when using a recrystallized alumina tube (a few minutes).

The reactants and reaction products were identified and quantified by using four complementary analytical techniques:

i. Online gas chromatography was used for the quantification of H_2 during the NH_3 oxidation in FR. It was equipped with a Carbosphere packed column (the carrier gas was argon), and a thermal conductivity detector (TCD). Argon was used as carrier gas to detect H_2 with a good sensitivity. The sampling was achieved in the outlet flow of the reactor using a sampling loop mounted on a six-way valve. Calibrations were performed using gaseous standards. The relative uncertainty in H_2 mole fraction is ±5%.

ii. On-line mass spectrometry (Omnistar from Pfeiffer) with ionization at 70 eV was used to detect NH_3, N_2, H_2O and O_2 in FR experiments. Sampling was carried out through a capillary tube directly connecting the reactor outlet and the analyzer under vacuum and sucking a constant flow. This technique requires the calibration of each species as there is no obvious relationship between their molecule structures and their calibration factors. Gaseous standards were used except for water, which was calibrated considering the reaction complete at the highest temperature. Note that this technique offers the possibility to follow the evolution of the different masses of interest as a function of the time and to

check for steady state conditions to be reached. The relative uncertainty in NH_3, N_2, H_2O and O_2 mole fractions was estimated to be ±10%.

iii. A continuous-wave cavity ring-down spectroscopy (cw-CRDS) cell coupled to the JSR by a sonic probe was used for NH_3 quantification. This technique is based on the absorption of species in the infrared, as for the FTIR technique. It is much more sensitive as the light path is much longer. It was already used in previous studies to quantify intermediates like hydrogen peroxide and HONO during the oxidation of fuels.[42,43] Ammonia has strong absorption lines in the wavenumber range 6637–6643 cm^{-1}, making the quantification accurate and providing a good sensibility. Fig. 3 displays an extract of a spectrum recorded during the present study under unreactive condition (φ = 1, T = 500 K). The whole spectrum recorded over the range 6637–6643 cm^{-1} is given in the ESI.† Two intense lines were used to quantify ammonia with a good sensitivity: 6641.33 and 6642.57 cm^{-1}. Cross sections needed for the calibrations were measured using data recorded under unreactive conditions. The relative uncertainty in NH_3 mole fraction detected by CRDS is ±10%.

iv. A dual channel NO_x chemiluminescence analyzer (Thermo Scientific Model 42i) was used for the detection of NO and NO_2 (but no NO_2 was detected in these experiments). The detection is based on the conversion of NO (with ozone) to an excited state of NO_2 that emits a chemiluminescent light when dropping to the ground state. On the first channel, the detection of nitric oxide is performed in a direct and independent way, whereas the second channel is dedicated to the measure of the total NO_x concentration. In this second channel, the sampled gas passes over a heated catalyst transforming nitrogen oxides to nitric oxide, NO, which is detected by chemiluminescence as in the first channel. NO_2 concentration is then deduced by substracting the concentration of NO from that of the total NO_x. Note that this analyzer is equipped by an ammonia trap to avoid the interference of this species. Calibrations were performed using gaseous standards. The relative uncertainty in NO mole fraction is ±5%, while that of NO_2 mole fraction is 10% since it is measured by difference.

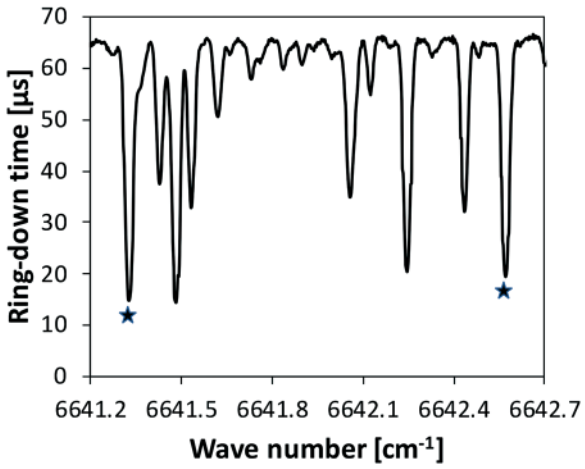

Fig. 3 Extract of the CRDS infrared spectrum recorded during the oxidation of ammonia under unreactive conditions (Φ = 1, T = 500 K). The two star symbols indicate the two intense lines which were used for the quantification of ammonia.

2.2 Theoretical methodologies

The rate constants of a specific set of reactions were determined theoretically. They were identified on the basis of a combined uncertainty and sensitivity analysis with respect to the explored experimental conditions as well as on the availability of previous experimental/theoretical studies for each of them. The adopted computational methodology is the *ab initio* transition state theory based master equation (ME) approach (AITSTME) that was recently implemented in the EStokTP software.[44] Electronic structure calculations for abstraction reactions were performed determining structures and vibrational frequencies at the M06-2X/aug-cc-pVTZ level and energies at the unrestricted CCSD(T)/aug-cc-pVTZ level, corrected for basis set size effect with the change of density fitted (DF) MP2 energies computed using aug-cc-pVQZ and aug-cc-pVTZ basis sets. Rate constants were estimated using variational transition state theory (VTST), as implemented in MESS[45] for both reactions exhibiting a saddle point on the minimum energy path (MEP) and for barrierless reactions. For abstraction reactions, the structure and energies of van der Waals wells on entrance and exit channels were determined at the M06-2X/aug-cc-pVTZ level of theory. For H-abstraction from NH_3 by OH, whose CCSD(T) wavefunction has a large T1 diagnostic of 0.056, the energy barrier was computed performing multireference calculations at the CASPT2/aug-cc-pVTZ level using a full valence (15e,12o) active space. Hindered rotors were treated in the 1D hindered rotor approximation with torsional potential energy surfaces (PES) determined at the M06-2X/6-311+G(d,p) level. Torsional motions were projected out of the Hessian when calculating harmonic frequencies.[44] Harmonic frequencies and MEP energies for barrierless reactions (NH_3 and HNO decomposition) were determined at the CASPT2/aug-cc-pVTZ level using a full valence active space. In the case of HNO decomposition, the wavefunction was state averaged over two states. All density functional theory (DFT) calculations were performed using the G09 computational suite,[46] while CCSD(T) and CASPT2 simulations were performed using Molpro 2010.[47]

2.3 Kinetic modeling

The development of the kinetic model was performed by following a hierarchical and modular approach, as originally conceived in the CRECK kinetic framework.[48] The core H_2/O_2 mechanism was adopted after the work of Metcalfe *et al.*[49] The NO_x module, foundation of the whole NH_3 mechanism, was taken from the work of Song *et al.*,[38] on turn based on the works of Faravelli, Frassoldati *et al.*[50,51] The major updates were performed on $HONO/HNO_2$ chemistry, after the recent work of Chen *et al.*[52] For all the species, the

thermodynamic properties were systematically updated using the database of Burcat and Ruscic.[53]

Ammonia submechanism was added on top of the NO_x module, and the critical reactions are summarized in Table 1. The parameters of reactions R1 to R6 and R28 were calculated through the fitting of the temperature-dependent rates obtained from the related theoretical calculations *via* a modified-Arrhenius format $k = AT^{\beta}\exp[-E_{act}/(RT)]$. In addition to the dissociation reaction calculated in this work, the reactions involving NH and NH_2 radicals were taken from Klippenstein *et al.*,[21] as well as NH_2OH chemistry. The only exception is represented by R7: in this case, the high-temperature estimation of Davidson *et al.*[12] was adopted (~35% smaller), which (extrapolated) showed a better agreement with lower-temperature experimental data. As for NH_2 reactions with NO and NO_2 (R16–R19), both rate constants and branching ratios between the product channels were taken following the guidelines of Glarborg *et al.*,[31] while for NH + NO (R26 and R27), the theoretical calculations of Haworth *et al.*[54] were fitted in the 1000–2600 K interval. For the higher N_2H_x chemistry, reactions were mainly taken from the review of Dean and Bozzelli,[55] including H-abstractions from N_2H_x compounds and N_2H_x dissociation.

At low temperatures ($T < 1200$ K), different works[31,33,34] highlighted the importance of H_2NO and HNO as key species. H_2NO is mainly formed from NH_2 interaction with O_2 and oxygenated species like HO_2 and NO_2. The delicate

Table 1 List of critical reactions in the NH_3 oxidation mechanism. Reaction rate expression is modified Arrhenius $k = AT^{\beta}\exp[-E_{act}/(RT)]$. Units are cm^3, cal, mol, K

ID	Reaction	A	β	E_{act}	Notes	Ref.
R1	$NH_3 \leftrightarrow NH_2 + H$	7.230×10^{29}	−5.316	110 862.4	0.1 atm	PW
		3.497×10^{30}	−5.224	111 163.3	1 atm	
		1.975×10^{31}	−5.155	111 887.8	10 atm	
		2.689×10^{31}	−4.920	112 778.7	100 atm	
R2	$NH_3 + H \leftrightarrow NH_2 + H_2$	1.963×10^{4}	2.854	8520.2		PW
R3	$NH_3 + OH \leftrightarrow NH_2 + H_2O$	1.559×10^{5}	2.372	118.9		PW
R4	$NH_3 + O \leftrightarrow NH_2 + OH$	4.430×10^{2}	3.180	6739.9		PW
R5	$NH_3 + HO_2 \leftrightarrow NH_2 + H_2O_2$	1.173×10^{0}	3.839	17 260.0		PW
R6	$NH_3 + O_2 \leftrightarrow NH_2 + HO_2$	1.415×10^{10}	1.285	55 224.0		PW
R7	$NH_2 + NH \leftrightarrow N_2H_2 + H$	1.500×10^{15}	−0.500	0.0		12
R8	$NH_2 + NH \leftrightarrow NH_3 + N$	9.600×10^{3}	2.460	107.0		21
R9	$NH + NH \leftrightarrow NH_2 + N$	5.700×10^{-1}	3.880	342.0		21
R10	$NH + NH \rightarrow N_2 + H_2$	6.260×10^{12}	−0.036	−160.9		21
R11	$NH + NH \rightarrow N_2 + H + H$	5.634×10^{13}	−0.036	−160.9		21
R12	$NH_2 + NH_2 \leftrightarrow NH_3 + NH$	5.640×10^{0}	3.530	550.0		21
R13	$NH_2 + O_2 \leftrightarrow HNO + OH$	2.900×10^{-2}	3.764	18 185.0		22
R14	$NH_2 + O_2 \leftrightarrow H_2NO + O$	2.600×10^{11}	0.487	29 050.0		22
R15	$NH_2 + HO_2 \leftrightarrow OH + H_2NO$	1.566×10^{13}	0.000	0.0		58
R16	$NH_2 + NO \leftrightarrow N_2 + H_2O$	2.600×10^{19}	−2.369	870.0		19
R17	$NH_2 + NO \leftrightarrow NNH + OH$	4.300×10^{10}	0.294	−866.0		19
R18	$NH_2 + NO_2 \leftrightarrow H_2NO + NO$	8.600×10^{11}	0.110	−1186.0		31
R19	$NH_2 + NO_2 \leftrightarrow N_2O + H_2O$	2.200×10^{11}	0.110	−1186.0		31
R20	$NH_2 + H \leftrightarrow NH + H_2$	4.000×10^{13}	0.000	3650.0		12
R21	$NH_2 + OH \leftrightarrow NH + H_2O$	9.600×10^{6}	1.970	670.0		59
R22	$NH_2 + O \leftrightarrow NH + OH$	7.000×10^{12}	0.000	0.000		55
	Duplicate	3.300×10^{8}	1.500	5076.8		55
R23	$NH_2 + O \leftrightarrow HNO + H$	1.500×10^{15}	−0.547	836.7		60
	Duplicate	7.730×10^{13}	−0.277	646.4		60
R24	$NH + O_2 \leftrightarrow HNO + O$	4.050×10^{11}	0.090	10 670.0		61
R25	$NH + O_2 \leftrightarrow NO + OH$	2.010×10^{15}	−1.380	5670.0		61
R26	$NH + NO \leftrightarrow N_2O + H$	5.328×10^{12}	0.026	−2893.9		54
R27	$NH + NO \leftrightarrow N_2 + OH$	3.635×10^{10}	0.361	−2844.3		54
R28	$HNO \leftrightarrow H + NO$	2.0121×10^{19}	−3.021	47 792.0	0.1 atm	PW
		1.8259×10^{20}	−3.008	47 880.0	1 atm	
		1.2762×10^{21}	−2.959	48 100.0	10 atm	
		5.6445×10^{21}	−2.855	48 459.0	100 atm	
		9.7111×10^{21}	−2.642	48 940.0	1000 atm	
R29	$HNO + O_2 \leftrightarrow NO + HO_2$	2.000×10^{13}	0.000	14 896.0		55
R30	$H_2NO + H \leftrightarrow HNO + H_2$	4.800×10^{8}	1.500	1559.8		55
R31	$H_2NO + H \leftrightarrow NH_2 + OH$	4.000×10^{13}	0.000	0.000		55
R32	$H_2NO + O \leftrightarrow HNO + OH$	3.300×10^{8}	1.500	486.8		55
R33	$H_2NO + OH \leftrightarrow HNO + H_2O$	2.400×10^{6}	2.000	1192.2		55
R34	$H_2NO + NO_2 \leftrightarrow HNO + HONO$	6.000×10^{11}	0.000	2000.0		57
R35	$H_2NO + NH_2 \leftrightarrow HNO + NH_3$	1.800×10^{6}	1.940	−580.0		55
R36	$H_2NO + O_2 \leftrightarrow HNO + HO_2$	2.300×10^{2}	2.994	16 500.0		31, 36
R37	$H_2NO + HO_2 \leftrightarrow HNO + H_2O_2$	3.360×10^{5}	2.000	−1434.0	Estimated	PW

competition between the different H-abstraction reactions on H_2NO drives the reactivity of the whole system, since abstraction by O_2 giving HNO and HO_2 (R32) activates the radical branching, while the remaining abstractors deplete H_2NO and hinder the branching process. Among them, the only reaction studied at a fundamental level is R36,[36] included by Glarborg *et al.* in their review[31] (as well as in the present work) with an activation energy lowered by 2.5 kcal mol^{-1}. Under the investigated conditions, the low temperature and high oxygen concentration resulting in high amounts of HO_2 make the related H-abstraction (R37) particularly important. Considering the known kinetic parameters evaluated for the H-abstraction by O_2, H-abstraction *via* HO_2 was estimated following the generalized methodology proposed by Ranzi *et al.*[56] to predict kinetic parameters for H-abstraction reactions from hydrocarbons. The obtained constant has a comparable activation energy to that proposed by Dean and Bozzelli,[55] but on average it is a factor ~9 smaller on a T = 500–1500 K interval. The remaining H-abstractions from H_2NO (R30–R35) were taken from the evaluations of Dean and Bozzelli,[55] or estimations from Glarborg *et al.*[57] Due to the high sensitivity of NH_3 reactivity to the H_2NO amount at low temperatures, an accurate evaluation of the remaining H-abstractions can be a useful development of this activity; this is especially true in relation to the most stable radicals (*i.e.* NH_2, NO_2) at low temperatures, for which Ranzi *et al.*[56] did not propose any correlation.

The complete kinetic mechanism is made up of 31 species and 203 reactions, and is provided as ESI† of this work in CHEMKIN format, together with thermodynamic and transport properties.

3 Results and discussion

3.1 Estimated rate constants

The rate constant of two barrierless decomposition reactions and five H-abstraction reactions were determined theoretically. In particular, the barrierless decomposition of ammonia into NH_2 + H and of HNO into NO + H were determined as a function of temperature and pressure solving the master equation, and then fitted in the PLOG format. Ammonia decomposition has been studied in literature both as a forward and backward (recombination) process. The high-pressure rate constant calculated in the present work for ammonia recombination has a slight temperature dependence, increasing from 1.7×10^{14} cm^3 mol^{-1} s^{-1} to 2.8×10^{14} cm^3 mol^{-1} s^{-1} going from 300 K to 2500 K. These values are in reasonable agreement with the temperature independent value 1.6×10^{14} cm^3 mol^{-1} s^{-1} suggested by Glarborg *et al.*[31] The pressure-dependent decomposition rate is deep in its fall-off regime, so that the calculations are significantly affected by the inter molecular collisional energy transfer model adopted in the ME simulations. The experimental literature reports either experimental measurements of ammonia decomposition at high temperatures (higher than 2000 K)[12,58] or of NH_2 + H recombination rates at room temperature, but a systematic temperature- and pressure-dependent study is not available to the authors' knowledge.[62,63] In order to fit both high- and low-temperature data sets, a single exponential energy transfer model was adopted, with a ΔE_{down} of 130 $(T[K]/298)^{0.8}$ cm^{-1}. At 1 atm, the calculated rate constant is about a factor of 2 slower than the Davidson *et al.*[12] high temperature experimental decomposition rate, a factor of 2 larger than the high-temperature Baulch recommendation,[58] and in excellent agreement with the recent recombination measurement of Altinay and MacDonald,[63] on whose data ΔE_{down} was fitted in the present study. Experimental and theoretical data are compared in Fig. 4.

The rate constant for HNO decomposition was determined using the same ΔE_{down} value used for NH_3. The calculated high-pressure H + NO recombination rate is comprised

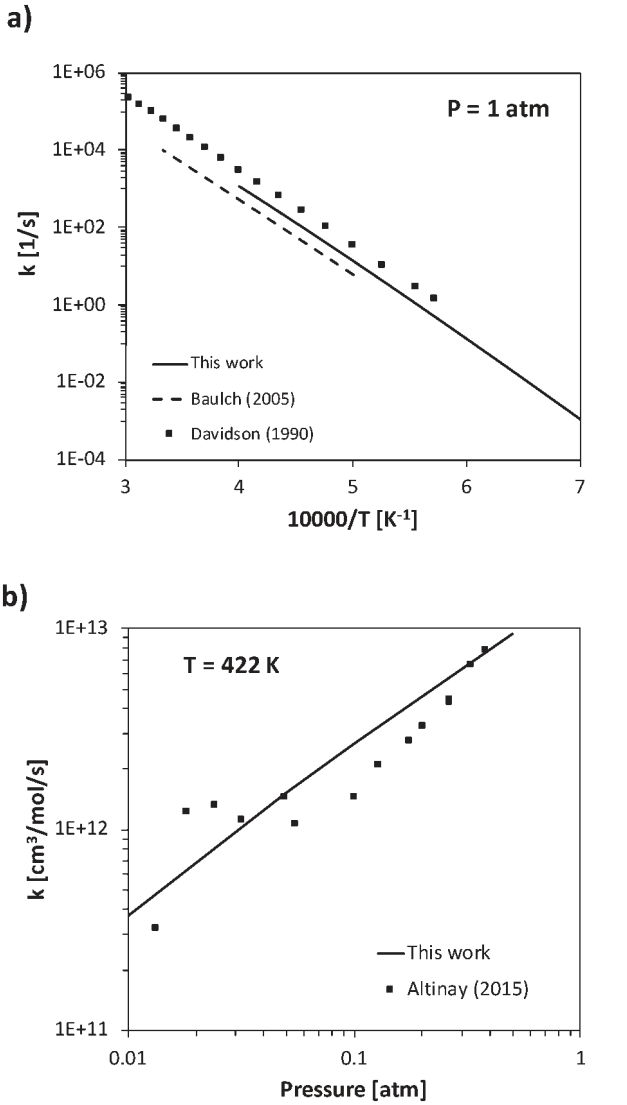

Fig. 4 Rate constant calculated a) for ammonia decomposition at 1 atm and b) NH_2 + H recombination at 422 K compared with experimental data.[12,58,63]

between 2.3×10^{14} cm^3 mol^{-1} s^{-1} and 1.9×10^{14} cm^3 mol^{-1} s^{-1} in the 300–2500 K range, thus in reasonably good agreement with the recommendation of Tsang and Herron[64] (between 1.2×10^{14} cm^3 mol^{-1} s^{-1} and 0.6×10^{14} cm^3 mol^{-1} s^{-1}), which has a large uncertainty factor of 5. The low-pressure recombination rate constant is compared with experimental data in Fig. 5. While the experimental data at room temperature are slightly overestimated, the agreement at temperatures higher than 500 K is quite good and fits very well with the data of Glarborg *et al.*,[65] which suggests that the pressure dependence is well caught by the adopted energy transfer model.

Rate constants were calculated for the five H-abstraction reactions from NH_3 by H, OH, $O(^3P)$, HO_2, and O_2. The calculated abstraction rate constants are in general within a factor of 2 from experimental measurements, when available. This is for example the case for H-abstraction by H, where the calculated rate constant is about a factor of 1.7 larger than that measured by Sutherland and Klemm[69] and Sutherland and Michael,[11] in the 750–1770 K temperature range. Also in the case of H-abstraction by OH, the agreement with literature data is quite good,[70–72] well within a factor of 2, as shown in Fig. 6. The energy barrier calculated at the CASPT2 level is 2.2 kcal mol^{-1}, thus about 1 kcal mol^{-1} smaller than the 3.2 kcal mol^{-1} determined at the CCSD(T) level, which is consistent with the multireference character of this reaction. A larger disagreement is observed for H-abstraction by $O(^3P)$. The calculated rate constant underestimates the experimental measurements of Sutherland *et al.*[73] by about a factor of 2.7 at 800 K. However, the disagreement decreases significantly with temperature, becoming just a factor of 1.2 at 1500 K. This suggests that the calculated energy barrier is probably overestimated, as was also suggested by Klippenstein *et al.*[21] in the study of this reaction channel for their CCSD(T) level energy barrier. It should be noted that, for this reaction channel, the electronic degeneracy of the transition state was assumed to be 6, as the ground and excited state in $O(^3P)$ abstraction reactions are nearly degenerate, as observed in a recent study of this reaction class.[74]

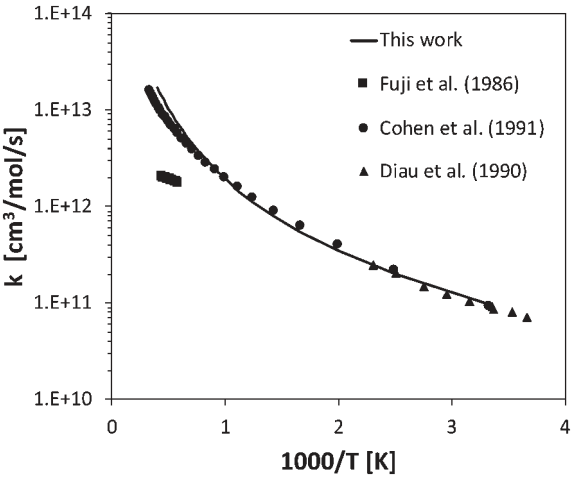

Fig. 6 Rate constant calculated for H-abstraction by OH on NH_3 compared with selected experimental data.[70–72]

For the H-abstraction channels by HO_2 and O_2, no literature reference is available, so that it is difficult to estimate their uncertainty. The rate constant estimation protocol adopted here is essentially the same as used in the EStokTP benchmark study,[44] where it was found that for abstraction reactions the uncertainty was smaller than a factor of 2 when compared to a large experimental data set. Considering the multireference character of several of the investigated reactions, it is though reasonable to assume that, under combustion conditions, the uncertainty factor of these rates may be up to a factor of 3.

For H-abstraction from NH_3 by O_2, previous works are available on the reverse reaction rate constant, below 500 K (Fig. 7). The photochemical study of Sarkisov *et al.*[75] estimated an overall rate coefficient of 4.5×10^{13} cm^3 mol^{-1} s^{-1} for the reaction $NH_2 + HO_2 \rightarrow$ products at 300 K, while Baulch *et al.*[76]

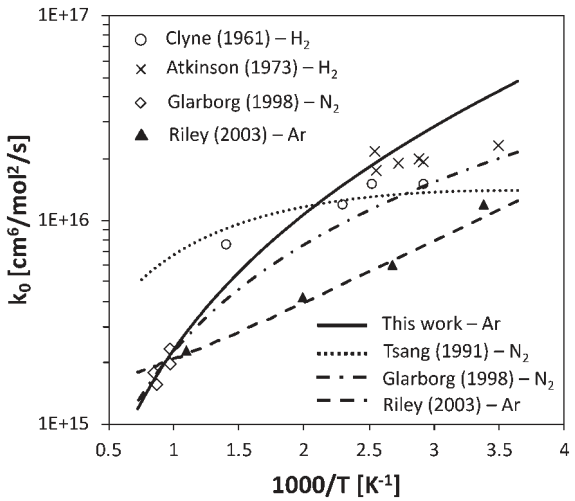

Fig. 5 Low-P recombination rate constant of the H + NO reaction, for different bath gases, compared with selected literature data.[64–68]

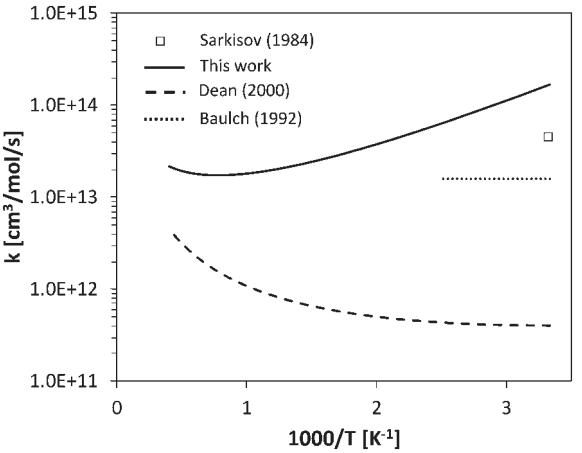

Fig. 7 Comparison between calculated rate constant and literature data[55,75,76] for reverse H-abstraction by O_2 on NH_3.

recommended a value of 1.6×10^{13} cm^3 mol^{-1} s^{-1} between 300 K and 400 K. The fit of the reverse H-abstraction obtained in this work overestimates the value of Sarkisov *et al.*[75] at room temperature by a factor of 2. Anyway, the previous evaluations of Dean and Bozzelli[55] and Sumathi *et al.*[77] underestimate the low-temperature data by orders of magnitude. This confirms the significant uncertainty existing in the theoretical evaluation of such an important step in the NH_3 oxidation mechanism.

The calculated rate constants are included in Table 1 and in the CHEMKIN format as ESI† to this paper. Input files for the MESS calculations, thus inclusive of energy barriers, stationary points geometries, and of the variational analysis results are also reported as ESI.†

3.2 NH_3 oxidation: experiments and kinetic analysis

The gas-phase oxidation of ammonia was investigated under a wide range of operating conditions: following a hierarchical approach, pyrolysis conditions were first considered, followed by high-temperature (T) oxidation, then intermediate- and low-temperatures with variable pressure (P), residence time (τ) and equivalence ratio (Φ), as shown in Table 2. In the following, the new experimental results collected in jet stirred and flow reactors are shown, and analyzed using the newly-developed kinetic model in order to explain the dynamics of conversion from NH_3 to final products. The full validation of the mechanism against the case studies listed in Table 2 is provided in the ESI.† For the sake of compactness, only selected cases are analyzed and discussed to highlight the main features of ammonia.

3.2.1 Jet stirred reactor. Experiments for NH_3 oxidation in JSR were carried out with helium as bath gas, by oxidizing 500 ppm of ammonia with 2% and 4% oxygen, respectively. Considering a global reaction $4NH_3 + 3O_2 = 2N_2 + 6H_2O$, the corresponding Φ values are 0.0188 and 0.0093. Results are shown in Fig. 8, with regard to NH_3 and NO mole fractions. NO_2 was not experimentally detected, in agreement with the simulations predicting maximum values of ~1.5 ppm.

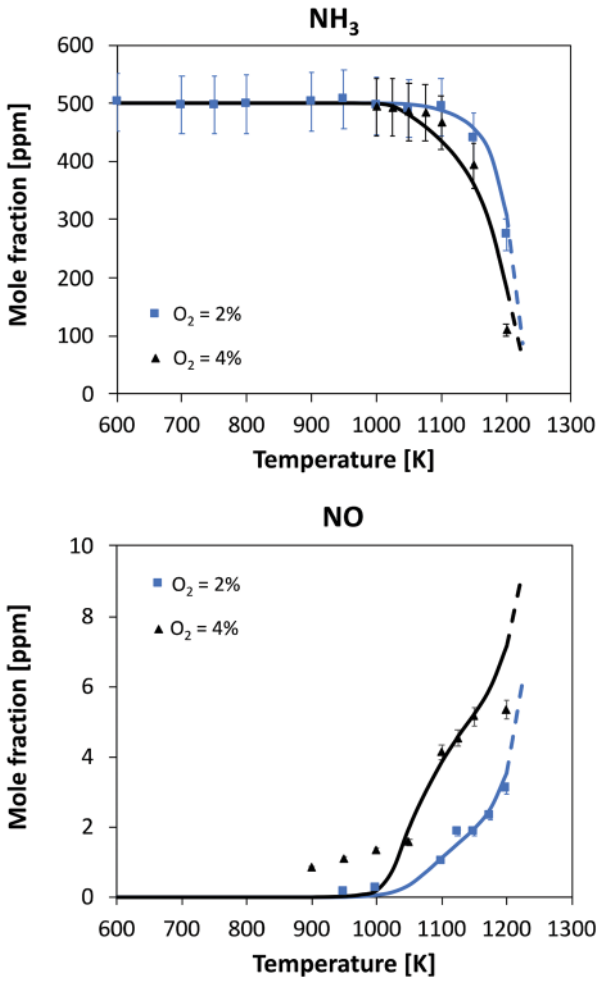

Fig. 8 Oxidation of 500 ppm of NH_3 in a JSR. Experimental and modeling results. P = 800 torr. τ = 1.5 s. Dashed lines: model extrapolation beyond the maximum reactor temperature.

Considering the highest oxygen concentrations, the reaction starts at relatively high temperatures, *i.e.* 1100 K and 1025 K with 2% and 4% oxygen, respectively. In both cases, the increase in consumption rate is very slow with

Table 2 Configurations and operating conditions investigated for NH_3 pyrolysis and oxidation

System	Composition	Operating conditions	T	P	Ref.
JSR	$NH_3/O_2/He$	500 ppm NH_3, Φ = 0.01–0.02, τ = 1.5 s	500–1200 K	106.7 kPa	PW
	$NH_3/NO/O_2/He$	500–1000 ppm NH_3, 500–1000 ppm NO, Φ = 0.1–2, τ = 0.1 s	1100–1450 K	1 atm	78
	$NH_3/NO/O_2/N_2$	960–10 800 ppm NH_3, 400–3000 ppm NO, O_2 = 0.8–6%, $\tau = 374/T$[K] s	950–1450 K	1 atm	79
FR	$NH_3/O_2/He$	1000 ppm NH_3, Φ = 0.375, τ = 50 ms	1200–2000 K	126.7 kPa	PW
	$NH_3/O_2/N_2$	242 ppm NH_3, O_2 = 10%, $\tau = 339/T$[K] s	850–1250 K	1 atm	35
	$NH_3/O_2/N_2$	729 ppm NH_3, Φ = 1.23, variable τ	450–925 K	30–100 bar	36
	$NH_3/O_2/N_2$	800 ppm NH_3, 2.5% O_2, $\tau = 71/T$[K] s	950–1350 K	1.05 bar	80
ST	NH_3/Ar	2700–3000 ppm NH_3	2300–2800 K	0.8–1.1 atm	12
	NH_3/O_2/Ar	Ar = 98–99%, Φ = 0.5–2	1550–2500 K	1.4–30 atm	27
	$NH_3/N_2/O_2$	N_2/O_2 = 3.76 : 1, Φ = 0.5–2	1100–1600 K	20–40 bar	32
RCM	$NH_3/O_2/N_2$/Ar	5–12% NH3, Φ = 0.2–0.5	1000–1100 K	37–75 atm	33
	NH_3/O_2/Ar	Φ = 0.5–2, 70% Ar	1000–1130 K	40–60 bar	34
LFS	$NH3/N_2/O_2$	Φ = 0.7–1.65	298 K	1 atm	81
	$NH3/O_2$	Φ = 0.2–2	298 K	1 atm	82
	$NH3/N_2/O_2$	Φ = 0.6–1.5, 21–45% O_2	298 K	1–5 atm	83
BSF	NH_3/O_2	40–65% NH_3 – balance O_2, v = 60.5 cm s^{-1}	300 K	20 torr	84

temperature but it is opposite to the amount of oxygen: in the 4% case, initial NH_3 is halved after 150 K from the reactivity onset, while in the 2% case this occurs after 100 K from the start of consumption. The kinetic model is able to predict this behavior, and at temperatures higher than 1200 K, it predicts a higher conversion with 2% oxygen. No experimental data are available beyond T = 1200 K due to the mechanical resistance of the quartz reactor, but the trend before the maximum allowed temperature also suggests an inversion in reactivity. A satisfactory agreement can also be seen in NO prediction, although the experiments detect an earlier formation of NO with 4% oxygen (~1 ppm at T = 900 K, where NH_3 conversion is close to zero). The shape of both profiles is well predicted by the kinetic model: in particular, at higher temperatures NO yield is predicted to converge to comparable values, *i.e.* 2% of the initial nitrogen amount. Interestingly, with 4% O_2 the NO profile is predicted having a double inflection point, and this is also confirmed by experimental results.

In order to identify the different reaction pathways leading to NH_3 conversion and NO formation, reaction flux analyses were performed for two representative conditions, *i.e.* T = 1050 K and T = 1200 K with 4% initial oxygen, when NH_3 conversion is ~10% and ~70%, respectively. The diagrams shown in Fig. 9 highlight similarities and differences between the two cases.

The major paths converting NH_3 into N_2 pass through NH_2 interaction with NO *via* R16 and R17 product channels, the latter forming NNH on turn quickly decomposing to N_2. NO formation is governed by the formation of H_2NO *via* NH_2 reaction with HO_2 and NO_2, respectively. H_2NO is then oxidized to HNO and finally to NO (with a small fraction passing through HONO and its further decomposition). At T = 1050 K, the higher amounts of NO_2 caused by the abundance of HO_2 radicals in the system enhance NH_2 conversion *via* the two channels of the NH_2 + NO_2 reaction (R18 and R19), and promote an earlier reactivity. On the other hand, the presence of HO_2 radical has a further effect: the flux analysis shows that the initiation reaction R6 is actually reversed, *i.e.* it behaves like a termination. Therefore, since a higher O_2 concentration results in a higher HO_2 amount, the increase in reactivity with 4% initial O_2 is slower with temperature, until the mixture with 2% O_2 becomes more reactive.

At higher temperatures, several major differences must be pointed out. First of all, the smaller amounts of HO_2 radicals result in lower NO_2 mole fractions. Therefore, NH_2 + NO prevails over NH_2 + NO_2, and the relative weight of the branching channel R17 increases. Moreover, the high-temperature chemistry of NH_3 becomes important: the significant presence of OH and O opens new pathways, forming NH radical (R21) and HNO (R23), respectively. The former reacts with NO forming N_2 (R26 and R27), either directly or *via* N_2O, while its oxidation with O_2 (R24 and R25) ultimately forms NO, whether or not passing through HNO. On the other hand, the reaction with O (R23) allows

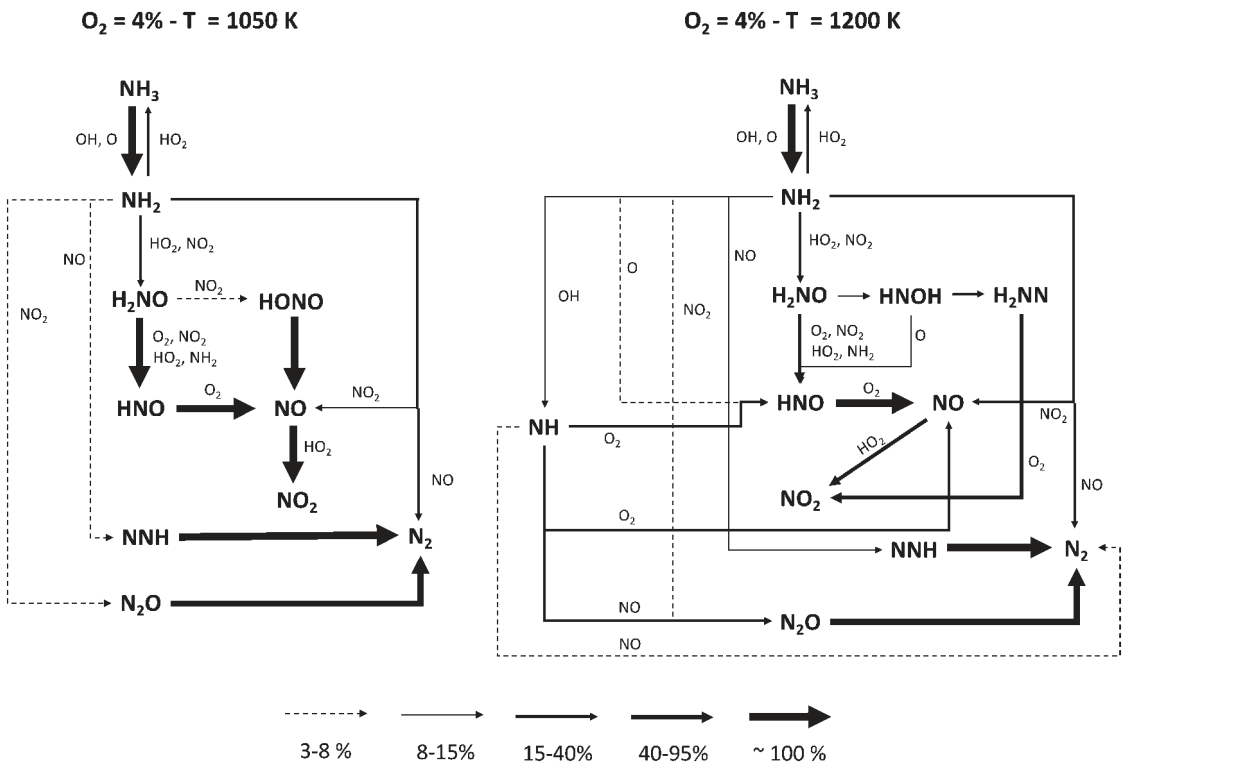

Fig. 9 Reaction flux analysis at different temperatures. Flux intensity is relative to the single molecule. For the sake of clarity, reactions between two N-molecules are reported only once.

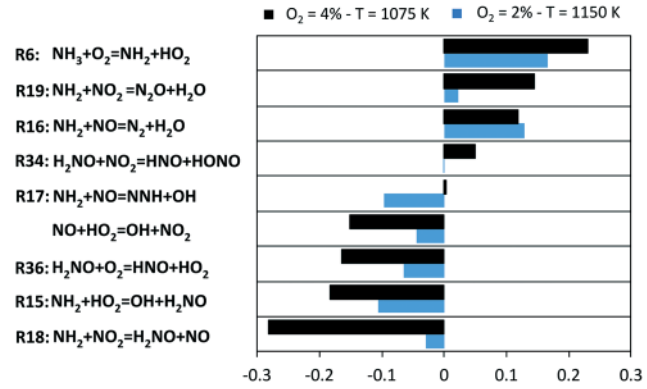

Fig. 10 Sensitivity coefficients to NH_3 mole fraction in two representative conditions of JSR experiments.

bypassing the H_2NO intermediate in the NH_3 oxidation pathway, in such a way that H_2NO becomes less and less important at higher temperatures.

The described picture is further confirmed by the sensitivity analysis of NH_3 mole fraction, used as representative of the system reactivity. Results are shown in Fig. 10 for two representative conditions, chosen such that a comparable conversion is attained (~10%).

Apparently, the system is controlled by the reactions involving HO_2 radicals, and for them, sensitivity coefficients are higher in the O_2 = 4% case. The H-abstraction by O_2 (R6), in spite of formally being an initiation, actually slows down the reactivity to a significant extent. Indeed, as shown in Fig. 9, R6 rather behaves as a termination step due to the high amounts of HO_2 and NH_2 radicals. On the other hand, H_2NO formation (R15) and successive oxidation (R36) enhance the overall reactivity. With 4% O_2, the NO_2 channels become critical in regulating NH_3 consumption: the formation of H_2NO (R18) gives a substantial contribution to the oxidation path (while a contrasting action is played by the termination channel R19). For this reason, the conversion of NO to NO_2 *via* HO_2 boosts NH_3 conversion. Indeed, the branching channel *via* NO (R17) becomes significant only at higher temperatures, as it can be noticed from the higher sensitivity coefficient of R17 in the O_2 = 2% case. In parallel, the channels involving NO_2 lose their crucial role with increasing temperature. Finally, the slowing effect of the remaining H-abstractions on H_2NO (especially NO_2) can be noticed especially at the lowest temperatures, because of the removal of active radicals from the low-temperature oxidation path.

Further examples of NH_3 oxidation in JSRs at atmospheric pressure can be found in the ESI,† where in particular the enhancing effect of NO addition is highlighted and the thermal DeNO$_x$ model is validated.

3.2.2 Flow reactor. Moving to higher temperatures, ammonia oxidation was then studied in a FR at temperatures above 1300 K. Experiments were carried out by injecting 1000 ppm NH_3 with 2000 ppm O_2 (Φ = 0.375), with a flow rate regulated in such a way to obtain a fixed residence time in the reactive zone, equal to 50 ms. Numerical simulations were performed by imposing the experimental temperature profile, and a variable flow rate (according to the set-point temperature) within the reactor. Fig. 11 shows the results for the major species. Ammonia conversion starts at around T = 1400 K, and is complete above 1500 K. In this temperature interval, H_2 is formed as an intermediate product, with an

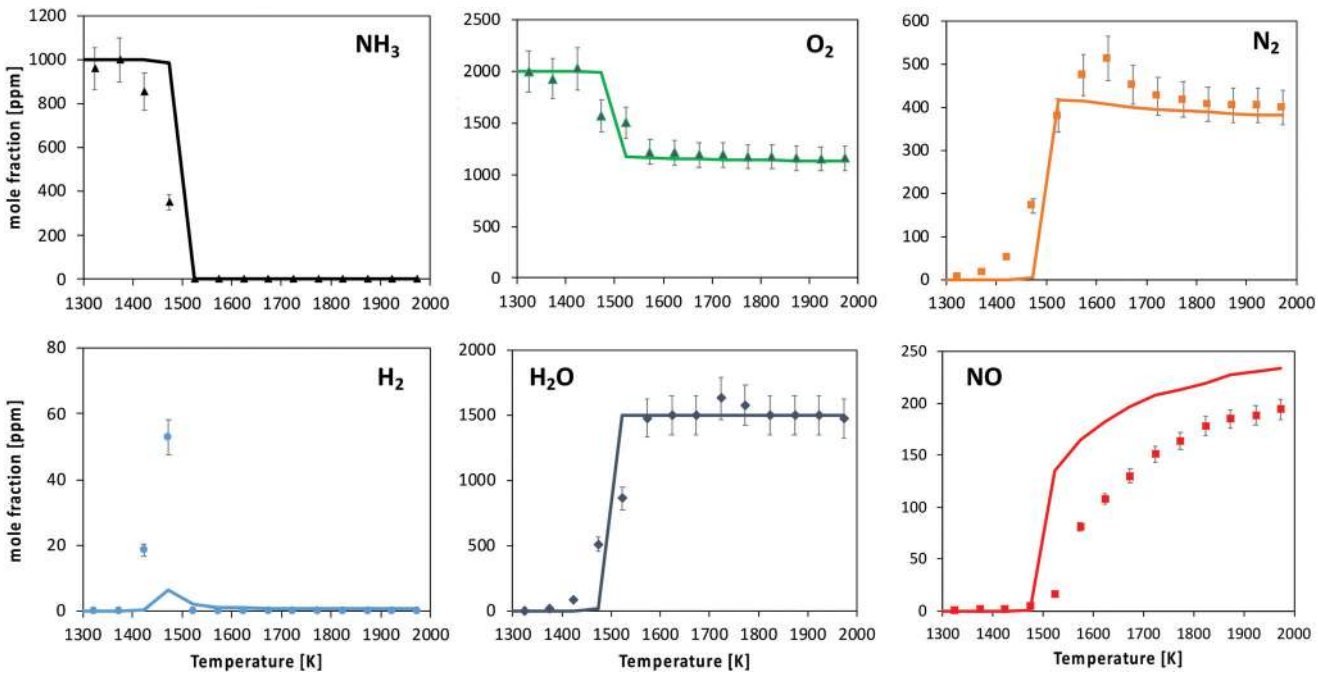

Fig. 11 Oxidation of 1000 ppm NH_3 with 2000 ppm O_2 in a FR. Experimental and modeling results. P = 950 torr. Average τ in the reactive zone is 50 ms.

observed peak of about 50 ppm. N_2 and NO are the major nitrogenated products, with the NO yield progressively increasing with temperature.

The kinetic model predicts the ignition temperature reasonably well, and consequently NH_3, O_2 and H_2O profiles. Anyway, the predicted consumption rate of ammonia and product formation is more abrupt than what was experimentally observed. The location of the H_2 peak is satisfactorily caught. The onset of NO formation is well reproduced in terms of temperature. However, the predicted NO/N_2 ratio is higher than the measured one: the shape of both profiles is well caught, but an overestimation of the NO mole fraction (about 20%) is observed at high-temperature.

Fig. 12 shows the routes leading to NO and N_2 formation at intermediate temperatures (*i.e.* straight after the reactivity onset). Compared to JSR, the pyrolysis mechanism plays a major role. The formation of N_2H_2 *via* R7 opens a new branching route through NNH, since overall an H atom is released in the conversion from NH_2 to N_2 (2 if N_2H_2 undergoes decomposition). The second branching route passes through HNO formation *via* NH_2 + O (R23), then releasing NO as final product.

The competition between the two paths becomes more apparent in the sensitivity analysis shown in Fig. 13, performed right after the reactivity onset, at a reactor length where NH_3 is almost fully consumed, and the reactions driving NO/N_2 selectivity can be distinguished. It can be observed that under such conditions, the path *via* HNO (R23 and R28) controls NO formation more than the path *via* N (thermal NO_x). On the other side, the major antagonists to NO selectivity are its reactions with NH and NH_2, respectively (R27 and R16), directly converting into N_2. Moreover, a higher formation of NH_2 (R3), precursor to the formation of both NO and N_2, enhances the formation of N_2 while having an

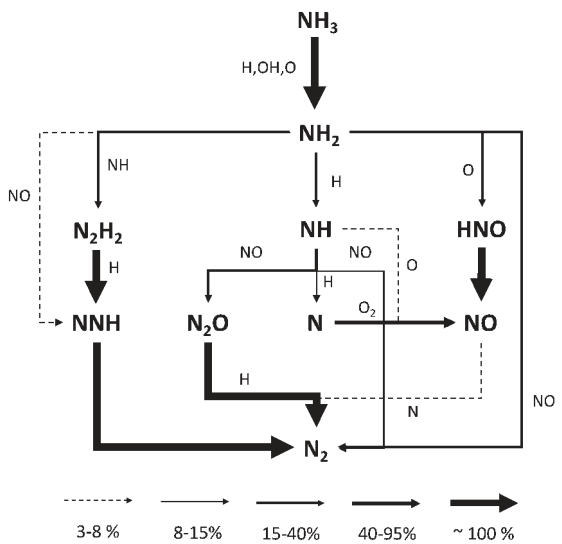

Fig. 12 Reaction flux analysis in FR at T = 1523 K and at a reactor length of 55 cm. Flux intensity is relative to the single molecule. For the sake of clarity, reactions between two N-molecules are reported only once.

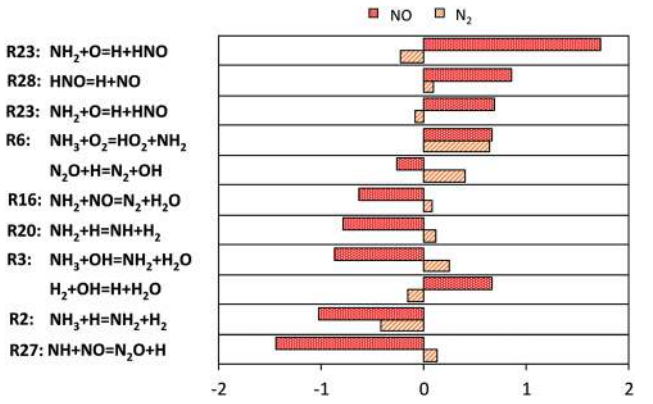

Fig. 13 Sensitivity coefficients to NO and N_2 mole fractions in FR case evaluated at T = 1523 K and at a reactor length of 58.5 cm (~100% ammonia conversion).

antagonistic effect on NO. This can be attributed to the combination of higher thermal $DeNO_x$ effects (R16) and NH formation *via* R20, on turn reacting again with NO and providing N_2.

3.2.3 Ignition delay times. The prediction ability of the kinetic model was assessed for the measurement of ignition delay times (IDTs) in a wide range of operating conditions, *i.e.* 1000 K < T_c < 2500 K and 1.4 atm < P_c < 60 atm, with different dilution levels. Due to the low reactivity of ammonia and longer IDTs, the presence of non-ideal, dynamic effects must be taken into account in the simulation of experimental data at both intermediate- and low-temperature conditions. Therefore, for the intermediate-temperature shock tube (ST) measurements,[32] the experimental pressure profile of the single experiments was converted into volume profile, starting from the arrival time of the reflected shock wave until the time point equal to 90% of the measured IDT, after which the volume was kept constant. Constrained-volume 0D simulations were then performed using the obtained profile. For the rapid compression machine (RCM) simulations,[34] the whole recorded pressure profile was converted into volume profile and used to perform constrained-volume 0D simulations. High-temperature datasets were instead simulated as homogeneous constant-volume 0D simulations.

Fig. 14 shows the results of 3 different equivalence ratios at various pressures. A satisfactory agreement can be observed for the high-temperature data of Mathieu and Petersen[27] in the whole operating range, with a slight underprediction under lean conditions. At intermediate temperatures (1100 K < T_c < 1600 K), the mechanism well reproduces the non-linear behavior of experimental data, due to pre-ignition effects. More significant deviations are can be seen at Φ = 2 and P_c = 40 bar. Yet, especially at the lowest temperatures (~1100 K), the experimental points at P_c = 20 and 40 bar are essentially overlapped. It must be also pointed out that the strongly irregular trend observed under stoichiometric and rich conditions is due to the different individual pressure histories recorded for the single points, which were used for the numerical simulations. The most

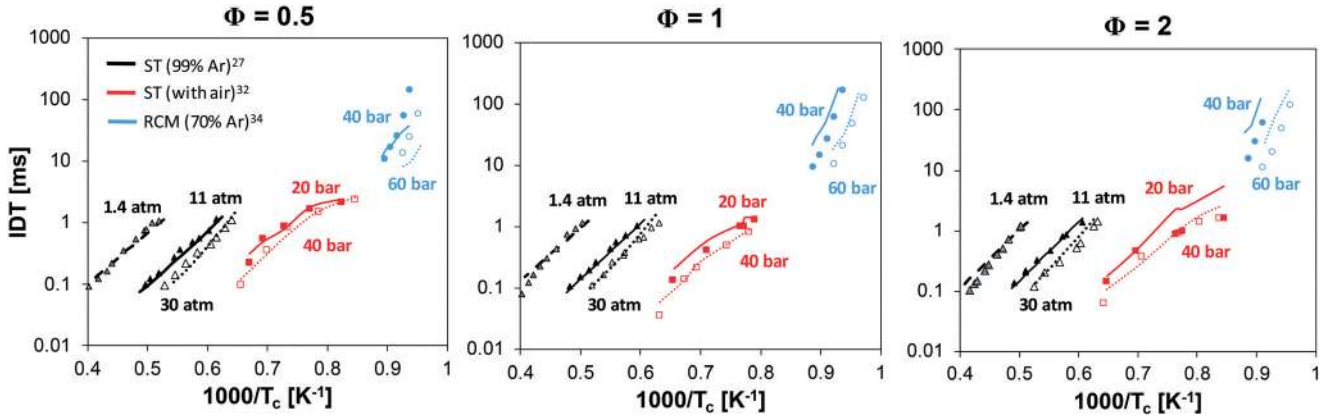

Fig. 14 Ignition delay times at low, intermediate and high temperature at variable Φ and P_c: experimental and modeling results.

critical predictions are observed at the lowest temperatures, *i.e.* when simulating RCM data by He *et al.*[34] where ignition is slightly underestimated at $\Phi = 0.5$, and overestimated at $\Phi = 1$ and especially $\Phi = 2$.

In order to understand the deviations under the richest conditions, a sensitivity analysis for OH mole fraction was performed under 3 representative conditions of the respective experimental campaigns at similar (high) pressures, at the beginning of the ignition phenomenon (~1% NH_3 conversion). Fig. 15 shows the related results: at low and intermediate temperatures, the key role of H_2NO is confirmed again, and the reactions promoting its formation (R15 and R18) and H-abstraction *via* O_2 (R36) drive the reactivity of the system. On the other side, the competition between branching and termination in the NH_2 + NO path (R16 and R17) has a primary role. On this regard, it is worth mentioning that the adopted rates for this path are pressure-independent. Recently, Klippenstein[24] reported a possible stabilization of reaction intermediates at higher pressures, resulting in an increase of the selectivity of the branching route R17. Therefore, considering such dependence could then improve the agreement with the data of He *et al.*,[34] although currently no pressure-dependent rates are available.

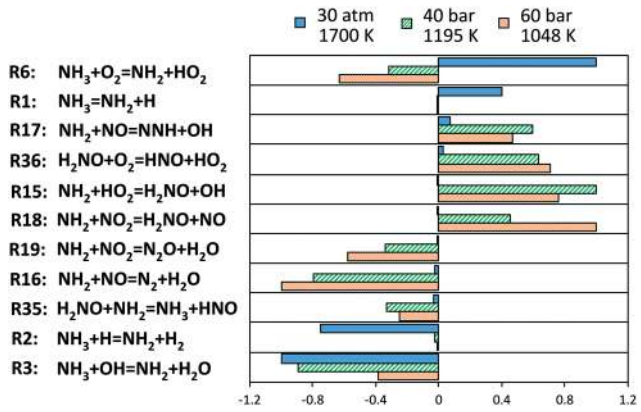

Fig. 15 Sensitivity coefficients to OH mole fraction at $\Phi = 2$, normalized with respect to the local maximum value, in correspondence of 1% ammonia conversion. The reaction H + O_2 = O + OH is omitted.

Finally, at higher temperatures, the H-abstraction on NH_3 by O_2 (R6) has an opposite effect with respect to low- and intermediate- temperature, and drives reactivity together with ammonia decomposition (R1), whilst H-abstractions by H and OH slow down the system, since subtracting active radicals from the related pool. In this case, the best agreement is found with the experiments.

3.2.4 Laminar flame speed. The prediction of laminar flame speed of ammonia flames is particularly critical because of the very low speed values compared to conventional hydrocarbons. This makes experimental campaigns more challenging, since with such low rates the relative weight of buoyancy forces is no longer negligible. Hayakawa *et al.*[85] showed that, when experimentally investigating spherically propagating flames of NH_3/air, buoyancy caused the movement of the flame center and the loss of the spherical assumption. This can affect the usability of such data for the validation of kinetic models, which is usually carried out by using 1D solvers. Therefore, in this work the capability of the developed mechanism in predicting laminar flame speed is verified by using the experimental data collected by Ronney[81] under microgravity conditions. For the sake of completeness, recent results obtained by Mei *et al.*[83] under gravity conditions, but in a more limited range of equivalence ratios are added. Moreover, Nakamura and Shindo[86] recently showed that, differently from methane flames, the effects of radiation heat loss on NH_3 flame speeds at ambient T and P were significant in a wide range of Φ, with a particular emphasis on lean and rich conditions. Therefore, radiation effects were accounted for through an optically-thin model.[87] Results are shown in Fig. 16, and highlight a very good agreement of the model at lean, stoichiometric and slightly rich conditions, with a small overestimation (less than 1 cm s^{-1}) for Φ close to the rich extinction (~1.7).

A deeper insight within the obtained results was obtained *via* sensitivity analysis to the flame speed (Fig. 17) for lean, stoichiometric and rich compositions, respectively. In all of

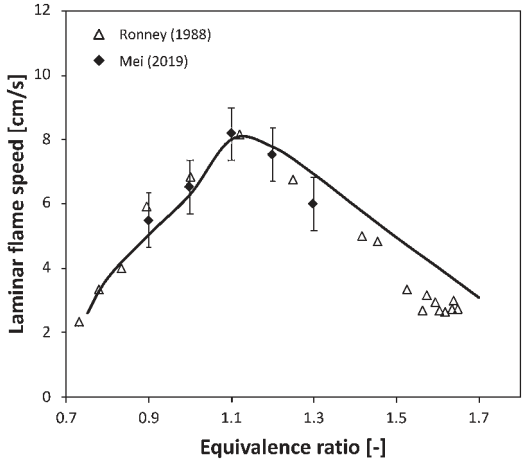

Fig. 16 Laminar flame speed of NH_3/air mixtures at P = 1 atm, T = 298 K.

them, it can be noticed that the competition between branching and termination of the NH_2 + NO reaction is again crucial (R16 and R17), but above all the production of H radicals *via* NH_2 + NH (R7) is the most enhancing path. HNO dissociation, which was studied in this work (R28), is also an important step under lean and stoichiometric conditions. Anyway, the most peculiar result is the inhibiting effect of R23, in spite of its production of H radicals. This can be attributed to the removal of NH_2 radicals from the just mentioned branching path R17 as well as R7. In addition, such path removes O radicals from the usual branching paths of the core H_2/O_2 mechanism. A more accurate estimation of R23 is then a critical milestone of the ammonia mechanism, and to the authors knowledge, the only temperature-dependent theoretical estimations of such constant were obtained by Bozzelli and Dean[88] and Sumathi *et al.*[60] (used in this work), differing from each other by a factor or ~1.4 at 1000–2000 K. R23 also had a boosting effect on the production of NO at intermediate and high-temperatures in flow reactor (Fig. 11 and 13), as already pointed out by Glarborg *et al.* in their review.[31] Therefore,

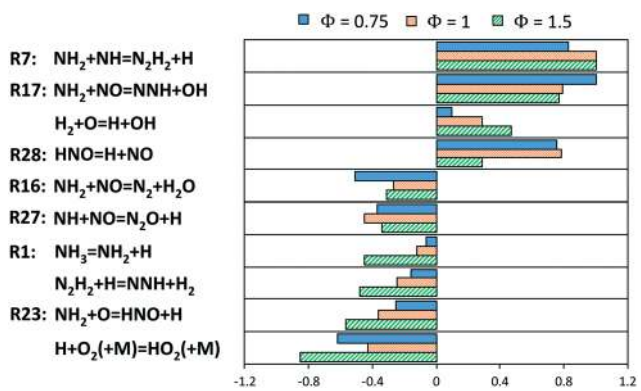

Fig. 17 Sensitivity coefficients (normalized with respect to the maximum value) to laminar flame speed at T = 298 K and P = 1 atm for different Φ. The reaction H + O_2 = O + OH is not reported.

considering the role of R23 within the current mechanism, the accuracy of those two datasets is someway competitive.

A more complete validation of the kinetic mechanism in terms of laminar flame speed predictions, with different oxidizer compositions can be found in the ESI.†

4 Conclusions

The renewed interest raised by NH_3 combustion in the recent years has made available a significant amount of experimental data, characterizing its reactivity in a wide range of operating conditions. Yet, a comprehensive understanding of its kinetic behavior is still an open challenge, especially at low-temperature (T < 1200 K) and under diluted conditions, on which the combustion community is devoting a significant effort because of the potentially lower NO_x emissions. In this work, this topic was addressed through a combined experimental and theoretical approach, able to shed light on the kinetic behavior of ammonia affecting low-temperature, diluted conditions. New experimental data were collected in jet-stirred and flow reactors at pressure close to atmospheric, in such a way to cover the whole range of temperatures (500–2000 K). In order to interpret these results, a theoretical analysis was performed to evaluate some of the most critical steps in the pyrolysis and oxidation mechanisms. By means of sensitivity analysis and literature review, the most critical reaction steps, not yet systematically investigated either experimentally or theoretically, were identified. Thus, the rate constants for ammonia decomposition, H-abstractions and the dissociation of the HNO intermediate were evaluated and included in a comprehensive kinetic model, built up following a first-principles approach, and incorporating the state-of-the-art kinetic rates.

The kinetic analysis of the low-temperature experiments allowed the identification of a peculiar behavior. Up to ~1200 K, the high amount of HO_2 radicals present in the system results in the inversion of the initiation *via* O_2, *i.e.* NH_3 + O_2 = NH_2 + HO_2 (recalculated in this work) acting instead as a termination step. Therefore, the reactivity of the systems is shifted to higher temperatures, and is distributed in a wider temperature range with increasing O_2 concentration. The key role of H_2NO was highlighted, as already reported in the literature, and the related H-abstractions by O_2, HO_2, NH_2 and NO_2 were found to affect reactivity at the lowest temperatures.

The comprehensiveness of the kinetic mechanism was also verified in the prediction of ignition delay time and flame propagation, where the key role of the newly-introduced kinetic rates was confirmed. At higher pressures and low temperatures, H_2NO was found to play a pivotal role in controlling ignition delay time. In this regard, theoretical work for the estimation of the H-abstractions on H_2NO and the effect of pressure on NH_2 + NO selectivity could further improve the predictability of the kinetic model in such conditions. Lastly, the prediction of laminar flame

speeds highlighted the key, decelerating effect of the reaction $NH_2 + O = HNO + H$, which promotes instead NO formation at high temperature, as found out in the analysis of flow reactor experiments. Further theoretical study on it can be useful for a more accurate, temperature-dependent re-evaluation of this step.

Nomenclature

Roman symbols

P Pressure [Pa]
T Temperature [K]

Greek symbols

τ Residence time [s]
Φ Equivalence ratio [–]

Acronyms

BSF	Burner-stabilized flame
DFT	Density functional theory
FR	Flow reactor
IDT	Ignition delay time
JSR	Jet-stirred reactor
LFS	Laminar flame speed
ME	Master equation
NO_x	Nitrogen oxides
PES	Potential energy surface
ppm	Parts per million
PW	Present work
RCM	Rapid compression machine
ST	Shock tube
VTST	Variational transition state theory

Subscripts

c After compression

Conflicts of interest

The authors declare no conflicts of interest.

Acknowledgements

This work has been carried out under the financial support of the IMPROOF project (H2020-IND-CE-2016-17/H2020-SPIRE-S016) within the European Union Horizon 2020 research and innovation program (grant agreement no. 723706), and of the COST Action CM1404 "Chemistry of smart energy carriers and technologies". The authors are also grateful to Prof. Christine Rousselle (Université d'Orléans) for the fruitful discussions.

References

1 J. W. Erisman, M. A. Sutton, J. Galloway, Z. Klimont and W. Winiwarter, *Nat. Geosci.*, 2008, **1**, 636–639.
2 H. Kobayashi, A. Hayakawa, K. D. K. A. Somarathne and E. C. Okafor, *Proc. Combust. Inst.*, 2019, **37**, 109–133.
3 F. Jiao and B. Xu, *Adv. Mater.*, 2019, **31**, 1805173.
4 D. Miura and T. Tezuka, *Energy*, 2014, **68**, 428–436.
5 J. Ikäheimo, J. Kiviluoma, R. Weiss and H. Holttinen, *Int. J. Hydrogen Energy*, 2018, **43**, 17295–17308.
6 D. P. B. T. B. Strik, A. M. Domnanovich and P. Holubar, *Process Biochem.*, 2006, **41**, 1235–1238.
7 L. Appels, J. Baeyens, J. Degrève and R. Dewil, *Prog. Energy Combust. Sci.*, 2008, **34**, 755–781.
8 R. O. Arazo, D. A. D. Genuino, M. D. G. de Luna and S. C. Capareda, *Sustainable Environ. Res.*, 2017, **27**, 7–14.
9 M. Yumura, T. Asaba, Y. Matsumoto and H. Matsui, *Int. J. Chem. Kinet.*, 1980, **12**, 439–450.
10 J. V. Michael, J. W. Sutherland and R. B. Klemm, *Int. J. Chem. Kinet.*, 1985, **17**, 315–326.
11 J. W. Sutherland and J. V. Michael, *J. Chem. Phys.*, 1988, **88**, 830–834.
12 D. F. Davidson, K. Kohse-Höinghaus, A. Y. Chang and R. K. Hanson, *Int. J. Chem. Kinet.*, 1990, **22**, 513–535.
13 M. Yumura and T. Asaba, *Symp. Combust.*, 1981, **18**, 863–872.
14 R. M. Green and J. A. Miller, *J. Quant. Spectrosc. Radiat. Transfer*, 1981, **26**, 313–327.
15 J. A. Miller, M. D. Smooke, R. M. Green and R. J. Kee, *Combust. Sci. Technol.*, 1983, **34**, 149–176.
16 J. Bian, J. Vandooren and P. J. Van Tiggelen, *Symp. Combust.*, 1988, **21**, 953–963.
17 R. K. Lyon, *Environ. Sci. Technol.*, 1987, **21**, 231–236.
18 J. Park and M. C. Lin, *Int. J. Chem. Kinet.*, 1996, **28**, 879–883.
19 S. Song, R. K. Hanson, C. T. Bowman and D. M. Golden, *J. Phys. Chem. A*, 2002, **106**, 9233–9235.
20 M. S. Wooldridge, R. K. Hanson and C. T. Bowman, *Symp. Combust.*, 1994, **25**, 741–748.
21 S. J. Klippenstein, L. B. Harding, B. Ruscic, R. Sivaramakrishnan, N. K. Srinivasan, M. C. Su and J. V. Michael, *J. Phys. Chem. A*, 2009, **113**, 10241–10259.
22 S. J. Klippenstein, L. B. Harding, P. Glarborg and J. A. Miller, *Combust. Flame*, 2011, **158**, 774–789.
23 S. J. Klippenstein, L. B. Harding, P. Glarborg, Y. Gao, H. Hu and P. Marshall, *J. Phys. Chem. A*, 2013, **117**, 9011–9022.
24 S. J. Klippenstein, *Proc. Combust. Inst.*, 2017, **36**, 77–111.
25 J. A. Miller and C. T. Bowman, *Prog. Energy Combust. Sci.*, 1989, **15**, 287–338.
26 A. A. Konnov and J. De Ruyck, *Combust. Sci. Technol.*, 2000, **152**, 23–37.
27 O. Mathieu and E. L. Petersen, *Combust. Flame*, 2015, **162**, 554–570.
28 P. Dagaut, P. Glarborg and M. U. Alzueta, *Prog. Energy Combust. Sci.*, 2008, **34**, 1–46.
29 K. P. Shrestha, L. Seidel, T. Zeuch and F. Mauss, *Energy Fuels*, 2018, **32**, 10202–10217.
30 R. Li, A. A. Konnov, G. He, F. Qin and D. Zhang, *Fuel*, 2019, **257**, 116059.
31 P. Glarborg, J. A. Miller, B. Ruscic and S. J. Klippenstein, *Prog. Energy Combust. Sci.*, 2018, **67**, 31–68.
32 B. Shu, S. K. Vallabhuni, X. He, G. Issayev, K. Moshammer, A. Farooq and R. X. Fernandes, *Proc. Combust. Inst.*, 2019, **37**, 205–211.

33 M. Pochet, V. Dias, B. Moreau, F. Foucher, H. Jeanmart and F. Contino, *Proc. Combust. Inst.*, 2019, **37**, 621–629.
34 X. He, B. Shu, D. Nascimento, K. Moshammer, M. Costa and R. X. Fernandes, *Combust. Flame*, 2019, **206**, 189–200.
35 V. J. Wargadalam, G. Löffler, F. Winter and H. Hofbauer, *Combust. Flame*, 2000, **120**, 465–478.
36 Y. Song, H. Hashemi, J. M. Christensen, C. Zou, P. Marshall and P. Glarborg, *Fuel*, 2016, **181**, 358–365.
37 R. C. da Rocha, M. Costa and X. S. Bai, *Fuel*, 2019, 24–33.
38 Y. Song, L. Marrodán, N. Vin, O. Herbinet, E. Assaf, C. Fittschen, A. Stagni, T. Faravelli, M. U. Alzueta and F. Battin-Leclerc, *Proc. Combust. Inst.*, 2019, **37**, 667–675.
39 L. Marrodán, Y. Song, M. Lubrano Lavadera, O. Herbinet, M. De Joannon, Y. Ju, M. U. Alzueta and F. Battin-Leclerc, *Energy Fuels*, 2019, **33**, 5655–5663.
40 M. Pelucchi, S. Namysl, E. Ranzi, A. Frassoldati, O. Herbinet, F. Battin-Leclerc and T. Faravelli, *Proc. Combust. Inst.*, 2019, **37**, 389–397.
41 J. Villermaux, *Génie de la réaction chimique: conception et fonctionnement des réacteurs*, Tec & Doc Lavoisier, Paris, 2nd edn, revue et augmentée, 1993.
42 C. Bahrini, O. Herbinet, P. A. Glaude, C. Schoemaecker, C. Fittschen and F. Battin-Leclerc, *J. Am. Chem. Soc.*, 2012, **134**, 11944–11947.
43 L. Marrodán, Y. Song, O. Herbinet, M. U. Alzueta, C. Fittschen, Y. Ju and F. Battin-Leclerc, *Chem. Phys. Lett.*, 2019, **719**, 22–26.
44 C. Cavallotti, M. Pelucchi, Y. Georgievskii and S. J. Klippenstein, *J. Chem. Theory Comput.*, 2019, **15**, 1122–1145.
45 Y. Georgievskii, J. A. Miller, M. P. Burke and S. J. Klippenstein, *J. Phys. Chem. A*, 2013, **117**, 12146–12154.
46 M. J. Frisch, G. W. Trucks, H. B. Schlegel, G. E. Scuseria, M. A. Robb, J. R. Cheeseman, G. Scalmani, V. Barone, G. A. Petersson and H. Nakatsuji, *et al.*, *Gaussian 09, Rev. D.01*, Gaussian Inc., Wallingford, CT, 2010.
47 H. J. Werner, P. J. Knowles, G. Knizia, F. R. Manby and M. Schütz, *Molpro: a General-Purpose Quantum Chemistry Program Package*, 2010, http://www.molpro.net.
48 E. Ranzi, A. Frassoldati, R. Grana, A. Cuoci, T. Faravelli, A. P. Kelley and C. K. Law, *Prog. Energy Combust. Sci.*, 2012, **38**, 468–501.
49 W. K. Metcalfe, S. M. Burke, S. S. Ahmed and H. J. Curran, *Int. J. Chem. Kinet.*, 2013, **45**, 638–675.
50 T. Faravelli, A. Frassoldati and E. Ranzi, *Combust. Flame*, 2003, **132**, 188–207.
51 A. Frassoldati, T. Faravelli and E. Ranzi, *Combust. Flame*, 2003, **135**, 97–112.
52 X. Chen, M. E. Fuller and C. Franklin Goldsmith, *React. Chem. Eng.*, 2019, **4**, 323–333.
53 A. Burcat and B. Ruscic, *Third millennium ideal gas and condensed phase thermochemical database for combustion with updates from active thermochemical tables*, 2005, vol. ANL-05/20.
54 N. L. Haworth, J. C. Mackie and G. B. Bacskay, *J. Phys. Chem. A*, 2003, **107**, 6792–6803.
55 A. M. Dean and J. W. Bozzelli, in *Gas-Phase Combustion Chemistry*, 2000, pp. 125–341.
56 E. Ranzi, M. Dente, T. Faravelli and G. Pennati, *Combust. Sci. Technol.*, 1994, **95**, 1–50.
57 P. Glarborg, P. G. Kristensen, K. Dam-Johansen, M. U. Alzueta, A. Millera and R. Bilbao, *Energy Fuels*, 2000, **14**, 828–838.
58 D. L. Baulch, C. T. Bowman, C. J. Cobos, R. A. Cox, T. Just, J. A. Kerr, M. J. Pilling, D. Stocker, J. Troe, W. Tsang and others, *J. Phys. Chem. Ref. Data*, 2005, **34**, 757–1397.
59 S. H. Mousavipour, F. Pirhadi and A. Habibagahi, *J. Phys. Chem. A*, 2009, **113**, 12961–12971.
60 R. Sumathi, D. Sengupta and M. T. Nguyen, *J. Phys. Chem. A*, 1998, **102**, 3175–3183.
61 M. R. Talipov, S. L. Khursan and R. L. Saflullin, *J. Phys. Chem. A*, 2009, **113**, 6468–6476.
62 P. B. Pagsberg, J. Eriksen and H. C. Christensen, *J. Phys. Chem.*, 1979, **83**, 582–590.
63 G. Altinay and R. G. MacDonald, *J. Phys. Chem. A*, 2012, **116**, 1353–1367.
64 W. Tsang and J. T. Herron, *J. Phys. Chem. Ref. Data*, 1991, **20**, 609–663.
65 P. Glarborg, M. Østberg, M. U. Alzueta, D. J. Kim and J. A. Miller, in *Symposium (International) on Combustion*, 1998, vol. 27, pp. 219–226.
66 M. A. A. Clyne and B. A. Thrush, *Trans. Faraday Soc.*, 1961, **57**, 1305–1314.
67 R. Atkinson and R. J. Cvetanović, *Can. J. Chem.*, 1973, **51**, 370–372.
68 P. S. Riley, B. Cosic and A. Fontijn, *Int. J. Chem. Kinet.*, 2003, **35**, 374–380.
69 J. W. Sutherland and R. B. Klemm, *Kinetic studies of elementary reactions using the flash photolysis-shock tube technique*, 1987, vol. 16.
70 N. Cohen and K. R. Westberg, *J. Phys. Chem. Ref. Data*, 1983, **12**, 531–590.
71 N. Fujii, S. Uchida, H. Sato, S. Fujimoto and H. Miyama, *Bull. Chem. Soc. Jpn.*, 1986, **59**, 3431–3437.
72 E. W. G. Diau, T. L. Tso and Y. P. Lee, *J. Phys. Chem.*, 1990, **94**, 5261–5265.
73 J. W. Sutherland, P. M. Patterson and R. B. Klemm, *J. Phys. Chem.*, 1990, **94**, 2471–2475.
74 C. Cavallotti, F. Leonori, N. Balucani, V. Nevrly, A. Bergeat, S. Falcinelli, G. Vanuzzo and P. Casavecchia, *J. Phys. Chem. Lett.*, 2014, **5**, 4213–4218.
75 O. M. Sarkisov, S. G. Cheskis, V. A. Nadtochenko, E. A. Sviridenkov and V. I. Vedeneev, *Arch. Combust.*, 1984, **4**, 111–120.
76 D. L. Baulch, M. J. Pilling, C. J. Cobos, R. A. Cox, C. Esser, P. Frank, T. Just, J. A. Kerr, J. Troe, R. W. Walker and J. Warnatz, *J. Phys. Chem. Ref. Data*, 1992, **21**, 411–734.
77 R. Sumathi and S. D. Peyerimhoff, *Chem. Phys. Lett.*, 1996, **263**, 742–748.
78 P. Dagaut and A. Nicolle, *Proc. Combust. Inst.*, 2005, **30**, 1211–1218.
79 R. Rota, D. Antos, E. F. Zanoelo and S. Carrà, *Combust. Sci. Technol.*, 2001, **163**, 25–47.
80 T. Hulgaard and K. Dam-Johansen, *AIChE J.*, 1993, **39**, 1342–1354.

81 P. D. Ronney, *Combust. Sci. Technol.*, 1988, **59**, 123–141.
82 Q. Liu, X. Chen, J. Huang, Y. Shen, Y. Zhang and Z. Liu, *J. Hazard. Mater.*, 2019, **363**, 187–196.
83 B. Mei, X. Zhang, S. Ma, M. Cui, H. Guo, Z. Cao and Y. Li, *Combust. Flame*, 2019, **210**, 236–246.
84 D. I. Maclean and H. G. Wagner, in *Symposium (International) on Combustion*, 1967, vol. 11, pp. 871–878.
85 A. Hayakawa, T. Goto, R. Mimoto, Y. Arakawa, T. Kudo and H. Kobayashi, *Fuel*, 2015, **159**, 98–106.
86 H. Nakamura and M. Shindo, *Proc. Combust. Inst.*, 2019, **37**, 1741–1748.
87 M. F. Modest, *Radiative Heat Transfer*, 2nd edn, 2003.
88 J. W. Bozzelli and A. M. Dean, *J. Phys. Chem.*, 1989, **93**, 1058–1065.